J. Fluid Mech. (2006), *vol.* 568, *pp.* 55–76.
doi:10.1017/S002211200600259X Printed in the United Kingdom

Population trends of spanwise vortices in wall turbulence

By Y. WU AND K. T. CHRISTENSEN†

Department of Mechanical Science and Engineering, University of Illinois, Urbana, IL 61801, USA

(Received 20 May 2005 and in revised form 25 May 2006)

The present effort documents the population trends of prograde and retrograde spanwise vortex cores in wall turbulence outside the buffer layer. Large ensembles of instantaneous velocity fields are acquired by particle-image velocimetry in the streamwise–wall-normal plane of both turbulent channel flow at $Re_\tau \equiv u_*\delta/\nu = 570$, 1185 and 1760 and a zero-pressure-gradient turbulent boundary layer at $Re_\tau = 1400$, 2350 and 3450. Substantial numbers of prograde spanwise vortices are found to populate the inner boundary of the log layer of both flows and most of these vortices have structural signatures consistent with the heads of hairpin vortices. In contrast, retrograde vortices are most prominent at the outer edge of the log layer, often nesting near clusters of prograde vortices. Appropriate Reynolds-number scalings for outer- and inner-scaled population densities of prograde and retrograde vortices are determined. However, the $Re_\tau = 570$ channel-flow case deviates from these scalings, indicating that it suffers from low-Re effects. When the population densities are recast in terms of fractions of resolved prograde and retrograde spanwise vortices, similarity is observed for $100 < y^+ < 0.8\delta^+$ in channel flow and in both flows for $100 < y^+ < 0.3\delta^+$ over the Re_τ range studied. The fraction of retrograde vortices increases slightly with Re_τ beyond the log layer in both flows, suggesting that they may play an increasingly important role at higher Reynolds numbers. Finally, while the overall prograde and retrograde population trends of channel flow and the boundary layer show little difference for $y < 0.45\delta$, the retrograde populations differ considerably beyond this point, highlighting the influence of the opposing wall in channel flow.

1. Introduction

The results of many recent experimental and computational studies suggest that wall turbulence is populated by hairpin vortices that tend to streamwise-align into larger-scale coherent groups termed vortex packets. The phrase 'hairpin vortex' is used herein to describe both symmetric and asymmetric hairpin-, lambda- and arch-like structures that are composed of either one or two streamwise-oriented legs connected to a spanwise-oriented head whose rotation is of the same sense as the mean shear. (Spanwise vortices with rotation in the same sense as the mean shear, hairpin heads or otherwise, are hereafter referred to as 'prograde' spanwise vortices.) These structures are qualitatively consistent with the horseshoe vortex first proposed by Theodorsen

† Author to whom correspondence should be addressed: ktc@uiuc.edu

(1952). At low Reynolds number (Re), Smith (1984) reported the existence of hairpin vortices and suggested an organized alignment of these structures in the streamwise direction. Smith *et al.* (1991) later showed that hairpin vortices can regenerate from an existing vortex. Similar organization and regeneration was noted by Zhou *et al.* (1999) who studied the evolution of an initial hairpin-like structure in the mean turbulent field of a low-Re channel via direct numerical simulation (DNS). Given sufficient strength of the initial structure, multiple hairpin vortices were spawned both upstream and downstream of the initial structure, creating a coherent train of vortices. The legs of vortices residing in the log layer were commonly observed to extend below $y^+ \equiv y/y_* = 60$ (y_* is the viscous length scale), consistent with the near-wall quasi-streamwise vortex observations of Brooke & Hanratty (1993) and Schoppa & Hussain (1997), among others. Zhou *et al.* (1999) also observed a preference for asymmetric hairpins, with one leg often stronger than the other. The stereoscopic visualizations of Delo, Kelso & Smits (2004) complement these efforts by providing three-dimensional views of this organization at low Re. Their results highlight the contorted nature of the vortices that agglomerate to form larger-scale structures and further support the coupling between near-wall ejections and the passage of large-scale motions.

Head & Bandyopadhyay (1981) observed ramp-like patterns at the outermost edge of a turbulent boundary layer at higher Re and proposed these patterns to be the imprint of groups of hairpin vortices inclined away from the wall. More recent particle-image velocimetry (PIV) measurements at moderate Re in a turbulent boundary layer by Adrian, Meinhart & Tomkins (2000) provide evidence that hairpin structures occur throughout the outer layer and streamwise-align to create larger-scale vortex packets. The PIV data permitted visualization of this organization in the streamwise–wall-normal plane within the interior of the boundary layer, showing that packets occur throughout the outer region in a hierarchy of scales. This scale hierarchy is consistent with the mechanisms proposed by Perry & Chong (1982), and Tomkins & Adrian (2003) provide direct evidence of spanwise scale growth via merging on an eddy-by-eddy basis up to $y^+ = 100$ and propose scenarios by which this scale growth might manifest itself for $y^+ > 100$. Finally, the efforts of Liu, Adrian & Hanratty (2001) and Ganapathisubramani, Longmire & Marusic (2003) underscore the important role these large-scale motions play in log-layer transport processes.

While prograde spanwise vortices are often observed in the outer layer of wall turbulence, vortical motions with positive ω_z signatures, 'retrograde' spanwise vortices, are also known to exist. The flow-visualization studies of Falco (1977) in the streamwise–wall-normal plane of a turbulent boundary layer revealed counter-rotating vortex pairs at the outer edge of the boundary layer (spatially coincident retrograde and prograde spanwise vortex cores). These 'typical eddies' exhibited spatial characteristics consistent with localized ring-like structures (Klewicki *et al.* 1990). Subsequent efforts by Falco and co-workers determined that such structures often originate in the outer layer and advect into the near-wall region, initiating outer-/inner-layer interactions that can actively lead to the generation of near-wall structure, including hairpin structures (Falco 1977, 1983, 1991). This outer-/inner-layer interaction model is further supported by the recent efforts of Klewicki & Hirschi (2004) who consistently observed hairpin vortices and retrograde structures clustered in the neighbourhood of intense near-wall shear layers, with the influence of retrograde structures increasing with Reynolds number. Further, the aforementioned stereoscopic visualizations of Delo *et al.* (2004) revealed the presence of loops and

mushroom-like patterns which, if sliced in the streamwise–wall-normal plane, would exhibit retrograde and prograde signatures.

While the origin of retrograde spanwise vortices is not yet understood, several possibilities have been reported that link their formation to hairpin structures. Yang, Meng & Sheng (2001) used a passive mixing tab to generate trains of hairpin vortices in a laminar boundary layer and observed the formation of retrograde spanwise vortices just below and upstream of strong hairpin structures. Alternatively, the efforts of Moin, Leonard & Kim (1986), Melander & Zabuski (1988) and Smith *et al.* (1991) revealed that the legs of hairpin structures can, under certain conditions, pinch off and reconnect to form localized ring-like structures. Further, Tomkins & Adrian (2003) proposed the generation of isolated retrograde spanwise vortices via the spanwise interaction of hairpin structures. Finally, it is also possible that spatially coincident prograde and retrograde spanwise vortices may in fact belong to a single hairpin structure. Klewicki (1997) found that hairpin vortices can turn in the spanwise direction, yielding pairs of counter-rotating spanwise vortices associated with the legs of the hairpin. Alternatively, a hairpin structure with a slight omega shape around its shoulders and head can yield the signature of a spanwise retrograde vortex. If such a structure were sliced in the streamwise–wall-normal plane through one of its shoulders, a pair of prograde and retrograde structures may be revealed with the prograde core oriented above and downstream of the retrograde core since hairpins are normally inclined at roughly 45° from the wall. This signature is qualitatively consistent with the observations of Yang *et al.* (2001) although they do not address such a possibility.

The intent of the present effort is to document the population trends of prograde and retrograde spanwise vortices as a function of wall-normal position, Reynolds number and flow. PIV measurements are made in the streamwise–wall-normal plane of turbulent channel flow and a zero-pressure-gradient turbulent boundary layer. A vortex identification method is used to extract the resolved vortices from the background turbulence, facilitating detailed population studies of these structures.

2. Experiments

2.1. *Flow facilities*

The channel-flow facility utilized in this effort has a development length of 252δ (where $\delta = 25$ mm is the half-height of the channel) and an aspect ratio of 12:1. The working fluid of the facility is air and the flow is conditioned by a series of screens, a honeycomb and a contraction. The flow is then tripped upon entrance to the channel with 36-grit sandpaper, ensuring fully developed flow at the test section. Glass windows in the test section provide optical access from all directions while static pressure taps mounted along the length of the channel facilitate independent evaluation of the wall shear stress (τ_w). Fluid properties are assessed from measurements of the atmospheric pressure and fluid temperature using an ideal gas relation in concert with Sutherland's correlation for kinematic viscosity. These flow and fluid properties are then used to determine the friction velocity, $u_* \equiv (\tau_w/\rho)^{1/2}$, and the viscous length scale, $y_* \equiv \nu/u_*$, at each Reynolds number.

The turbulent-boundary-layer measurements are made under zero-pressure-gradient conditions in a low-turbulence, open-circuit boundary-layer wind tunnel. This facility has a documented turbulence intensity of 0.16% in the free stream and the boundary layer develops over a 6.1 m-long hydraulically smooth flat plate that has an elliptically shaped leading edge and is mounted 100 mm above the bottom surface of the

	Re_τ —	δ (mm)	U_∞ ($m\,s^{-1}$)	u_* ($m\,s^{-1}$)	y_* (μm)	Δx^+ —	Δy^+ —	No. of realizations	Symbol —
Channel	570	25.0	8.6	0.41	44.1	9.3	9.3	2000	□
	1185	25.0	19.0	0.86	21.1	9.7	9.7	2000	○
	1760	25.0	29.7	1.27	14.2	9.0	9.0	2000	▽
TBL	1400	87.4	6.5	0.25	62.4	10.9	10.9	2500	■
	2350	103.1	9.9	0.36	43.9	12.3	12.3	2500	●
	3450	96.0	16.1	0.56	27.8	11.2	11.2	2499	▼

TABLE 1. Experimental parameters: Re_τ, friction Reynolds number; δ, channel half-height/boundary-layer thickness; U_∞, channel centerline velocity/boundary-layer free-stream velocity; u_*, friction velocity; y_*, viscous length scale; Δx^+ and Δy^+, inner-scaled PIV vector spacings in streamwise and wall-normal directions, respectively.

457 mm-tall test section (Meinhart 1994). The flow is tripped far upstream of the measurement location and optical access to the boundary layer is provided from the side and below by float glass windows. Fluid properties are determined in the same manner as the channel-flow experiments; however, u_* and y_* are assessed using the Clauser chart method. Table 1 summarizes the relevant flow parameters for all flow conditions studied.

2.2. *Velocity measurements*

Particle-image velocimetry is used to measure instantaneous, two-dimensional velocity (u, v) fields in the streamwise–wall-normal (x, y) plane of turbulent channel and boundary-layer flows. The channel-flow measurements are made at $Re_\tau \equiv u_*\delta/\nu = 570$, 1185 and 1760 with a field of view of $1.3\delta \times \delta$ (streamwise × wall-normal) confined between the bottom wall and the centreline of the channel. The boundary-layer measurements are made at $Re_\tau = 1400$, 2350 and 3450 (equivalently $Re_\theta \equiv U_\infty\theta/\nu = 3870$, 8330 and 10 730, where θ is the momentum thickness and U_∞ is the free-stream velocity) with a field of view of $\delta \times \delta$ at the two lower Re and $1.45\delta \times \delta$ at the highest Re. The flows are seeded with 1 μm olive-oil droplets and the fields of view are illuminated with lightsheets formed from a pair of Nd:YAG lasers. The lightsheets have a spanwise thickness of $\Delta z \simeq 200$ μm and 500 μm in the channel and boundary-layer cases, respectively. A 1.3 k × 1 k pixel 12-bit CCD camera is used to image the particles in the channel-flow cases while the boundary-layer measurements are achieved with a 2 k × 2 k pixel 12-bit CCD camera at $Re_\tau = 1400$ and 2350 and a 4 k × 2.8 k pixel 12-bit CCD camera at $Re_\tau = 3450$. Time delays are selected to ensure a relative velocity measurement error of less than 1% in all cases.

The pairs of PIV images are subdivided into square interrogation windows and a larger second window is selected to minimize bias errors associated with loss of image pairs. The images are analysed using two-frame cross-correlation methods with 50% overlap to satisfy Nyquist's criterion and the second window is offset in the mean flow direction by the bulk displacement of the flow. Since our interest lies in studying the properties of smaller-scale spanwise vortices whose diameters appear to scale with y_* (Carlier & Stanislas 2005), the size of the first interrogation window is chosen such that the vector grid spacing at each Re_τ is consistent in inner units. To meet this requirement, the dimensions of the first interrogation windows are chosen to yield vector grid spacings, Δx and Δy, of approximately $9.0y_*$ for all three channel-flow Re_τ and $11y_*$ for the three boundary-layer Re_τ (see table 1). The instantaneous vector fields are then validated using standard deviation and local magnitude difference

comparisons to remove erroneous velocity vectors. The few holes generated by this validation process are filled either with alternative velocity choices determined during the interrogation or interpolated in regions where at least 50% of neighbours are present. Each vector field is then low-pass filtered with a narrow Gaussian filter to remove any noise associated with frequencies larger than the sampling frequency of the interrogation.

3. Vortex identification

Accurate assessment of the population trends of prograde and retrograde spanwise vortices requires the identification and extraction of such structures from the background turbulence. Galilean decomposition via removal of a fixed advection velocity from an instantaneous velocity field represents one method for uncovering vortices advecting at similar speeds and is often the best choice when one wishes to study the local motions induced by these structures. Unfortunately, since the advection velocity of a given vortex in a wall-bounded flow can depend upon its position relative to the wall, one must remove a broad range of advection velocities in order to reveal all embedded structure.

Alternatively, vortical structures can be identified through analysis of the local velocity-gradient tensor (Chong, Perry & Cantwell 1990; Zhou *et al.* 1999, for example). Swirling strength utilizes the imaginary part of the complex eigenvalue of the local velocity-gradient tensor (λ_{ci}) to reveal embedded structure (Zhou *et al.* 1999). Vortex identification via swirling strength is Galilean invariant and does not identify regions of intense shear that have no rotation. However, while swirling strength is adept at identifying vortices embedded in turbulent velocity fields, it does not yield the sense of the rotation. Therefore, a swirling-strength parameter of the form

$$\Lambda_{ci}(x, y) \equiv \lambda_{ci}(x, y)\frac{\omega_z(x, y)}{|\omega_z(x, y)|} \tag{3.1}$$

is introduced, where ω_z is the instantaneous fluctuating spanwise vorticity. This modified swirling strength is analogous to the one employed by Tomkins & Adrian (2003) in wall-parallel PIV planes and yields a clear distinction between vortices with counterclockwise and clockwise rotation (the phrase 'swirling strength' hereon refers to Λ_{ci}).

Figure 1 presents an example of vortex identification via swirling strength using an instantaneous channel-flow velocity field in the streamwise–wall-normal plane at $Re_\tau = 1185$. Galilean decomposition of this instantaneous field with an advection velocity of $0.8U_\infty$ (figure 1*a*) reveals only those spanwise vortices advecting at this speed, particularly in the region $0.1 < y/\delta < 0.3$. Contours of instantaneous Λ_{ci} are also shown in the background of figure 1(*a*). Clusters of non-zero Λ_{ci} are noted at all locations where swirling motions are present in the Galilean-decomposed velocity field as well as at numerous spatial locations where vortices are not apparent in the velocity field. One can confirm that all of these Λ_{ci} clusters represent embedded swirling motions by performing a local Galilean decomposition in the immediate vicinity of each Λ_{ci} cluster in figure 1(*a*). This local decomposition, shown in figure 1(*b*), confirms that all regions of non-zero Λ_{ci} are indeed associated with closed streamline patterns in the spirit of the definition of a vortex offered by Kline & Robinson (1989). Figure 1(*b*) also highlights the large populations of prograde and retrograde spanwise vortices that can exist in wall-bounded turbulence as 8 retrograde and 18 prograde vortices are identified in this realization. Finally, these cores represent

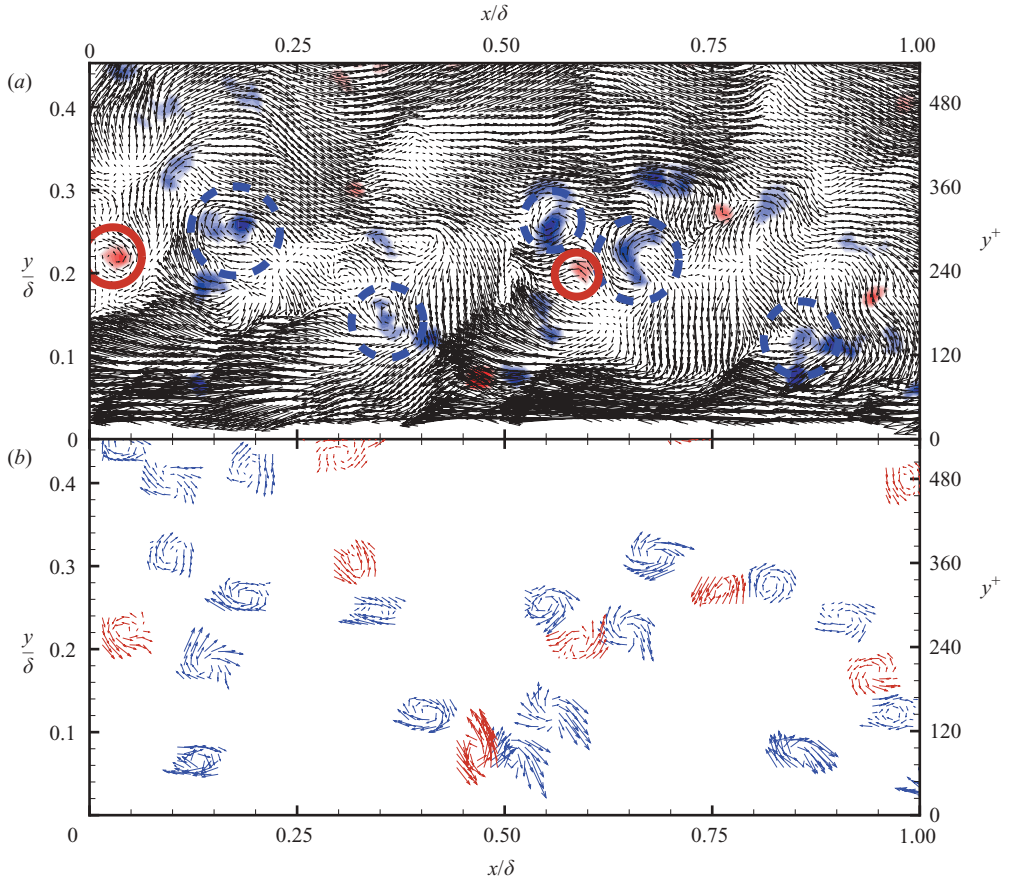

FIGURE 1. Example of vortex identification and extraction in an instantaneous, two-dimensional PIV velocity field acquired in turbulent channel flow at $Re_\tau = 1185$. (*a*) Galilean decomposition of the instantaneous velocity field at $U_c = 0.8U_\infty$ with contours of instantaneous Λ_{ci} in the background; (*b*) localized Galilean decomposition of vortices identified using Λ_{ci}. Retrograde spanwise vortices are presented in red and prograde vortices in blue.

spanwise sections of vortices since their orientations relative to the measurement plane cannot be determined from the two-dimensional fields.

A crucial consideration in the identification of vortical structures via Λ_{ci} is the threshold one selects for identifying the boundaries of the vortex sections (the example presented in figure 1 utilizes a threshold of $|\Lambda_{ci}(x, y)| \geqslant 1.5\Lambda_{ci}^{rms}(y)$). Nagaosa & Handler (2003) encountered similar issues in the identification of vortices in a DNS of turbulent flow in an open channel using Q, the second invariant of $\nabla \boldsymbol{u}$. They found that normalizing Q with its root-mean-square (RMS) at a given wall-normal location yielded probability density functions (p.d.f.s) of $\widetilde{Q}(x, y) = Q(x, y)/Q_{rms}(y)$ that were insensitive to y. Normalization by $Q_{rms}(y)$ is intuitive since it represents the characteristic magnitude of Q at a given wall-normal location about the mean of Q. After considering a range of thresholds, Nagaosa & Handler (2003) selected the threshold $|\widetilde{Q}| = 1$ which clearly identified vortical structures throughout their DNS realizations.

Since Q and λ_{ci} yield comparable vortex-identification results (Chakraborty, Balachandar & Adrian 2005), the selection of a universal Λ_{ci} threshold should

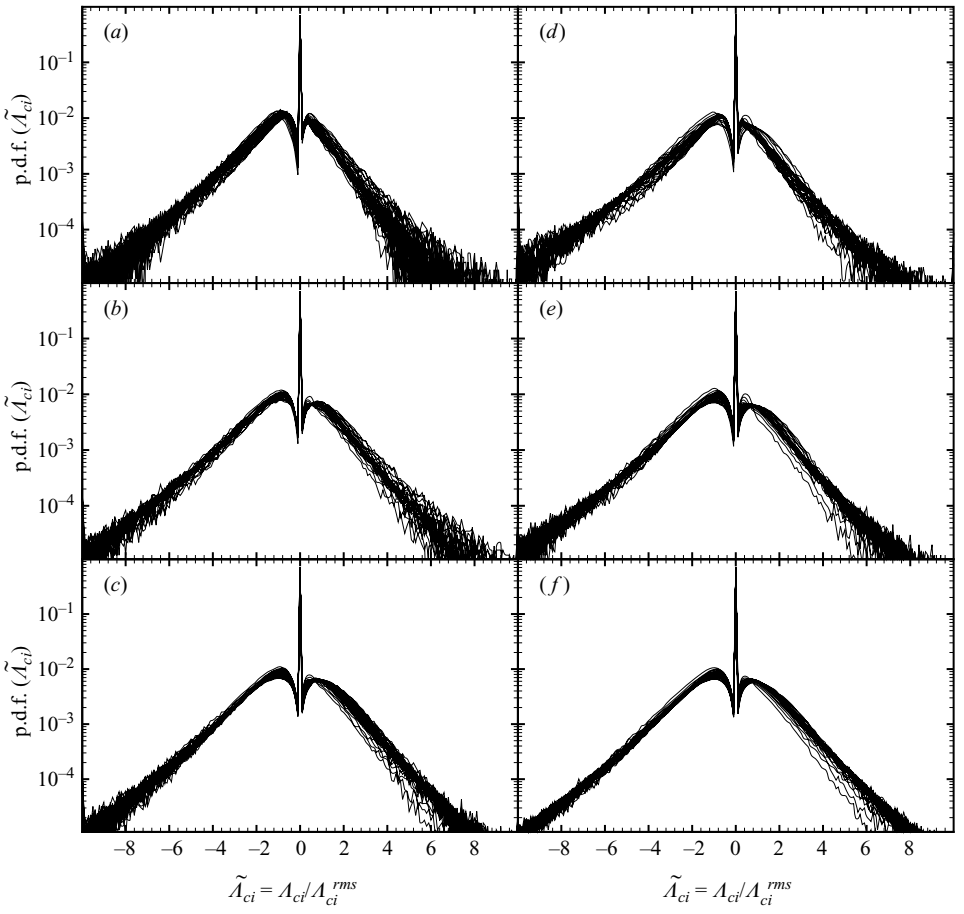

FIGURE 2. Probability density functions of $\widetilde{\Lambda}_{ci}$ for $100 < y^+ < 0.95\delta^+$. (*a–c*) Channel flow at $Re_\tau = 570$, 1185 and 1760, respectively; (*d–f*) boundary layer at $Re_\tau = 1400$, 2350 and 3450, respectively.

also be possible. Given that Λ_{ci} is highly intermittent since it is non-zero only within vortex cores (see figure 1*a*), the mean of Λ_{ci} is extremely small compared to its RMS. As such, $\Lambda_{ci}^{\rm rms}(y)$ is representative of the characteristic magnitude of Λ_{ci} within vortices at a given y and we therefore propose a normalized swirling strength of the form $\widetilde{\Lambda}_{ci}(x, y) = \Lambda_{ci}(x, y)/\Lambda_{ci}^{\rm rms}(y)$ as a basis for defining a universal threshold. Figure 2(*a–c*) presents p.d.f's of $\widetilde{\Lambda}_{ci}$ at several wall-normal locations for the $Re_\tau = 570$, 1400 and 1760 channel-flow cases, respectively, while figure 2(*d–f*) presents similar p.d.f's for the $Re_\tau = 1400$, 2350 and 3450 boundary-layer cases, respectively. These p.d.f's of $\widetilde{\Lambda}_{ci}$ are similar to those reported by Nagaosa & Handler (2003) for $\widetilde{Q}$ in terms of their relative insensitivity to y, particularly for $|\widetilde{\Lambda}_{ci}| < 4$. In addition, the Λ_{ci} p.d.f's also display both Reynolds-number and flow insensitivity, indicating that the selection of a universal $\widetilde{\Lambda}_{ci}$ threshold, independent of y, Re and flow, is possible. Since $\Lambda_{ci}^{\rm rms}(y)$ is the representative scale of non-zero $\Lambda_{ci}(y)$ (i.e. vortices), the threshold $|\widetilde{\Lambda}_{ci}| = 1$ is a natural starting point and was initially attempted in the present effort. However, this threshold yielded vortex sections with very jagged edges, indicating that it may be somewhat contaminated by the experimental noise associated with

differentiation of the PIV data. While the inclusion of such edge noise does not alter the vortex populations appreciably, most notably their Reynolds-number and wall-normal trends and their scalings, it does alter the space occupied by the cores which in turn modifies the quantitative values of their mean shear contributions presented later. We therefore settled on a slightly larger threshold of $|\widetilde{\Lambda}_{ci}| = 1.5$ which limits the influence of experimental noise associated with the calculation of $\nabla \boldsymbol{u}$ from the PIV measurements.

Beyond the choice of an appropriate swirling-strength threshold, the size of the smallest resolvable vortex section is inherently limited by the spatial resolution of the PIV measurements. As such, clusters of Λ_{ci} with fewer than three grid points across their span in both x and y satisfying $|\widetilde{\Lambda}_{ci}| \geqslant 1.5$ are not considered due to insufficient spatial resolution. Therefore, the spanwise vortices studied herein are necessarily limited to structures with cross-sectional lengths exceeding $18y_*$ and $22y_*$ in the channel-flow and boundary-layer datasets, respectively. The present analysis is also limited to the wall-normal region outside the buffer layer ($y^+ \gtrsim 100$) since the spatial resolution achieved is insufficient to fully resolve the flow beneath the log layer.

Finally, validation of this identification method is accomplished by comparing the average cross-sectional length scales of the identified vortex sections with the recent boundary-layer results reported by Carlier & Stanislas (2005) who used a Gaussian-vortex template as a vortex identifier. They report an average log-layer diameter range of $D = 40y_* - 50y_*$ at $Re_\theta = 8330$ averaged over both prograde and retrograde structures. For comparison, the area occupied by each vortex section in the current $Re_\tau = 2350$ ($Re_\theta = 8830$) boundary-layer ensemble is assessed, yielding a measure of its cross-sectional length, $L = \sqrt{A}$ (this length scale was chosen instead of assuming a circular cross-section and computing a diameter since the orientation of the vortices relative to the measurement plane is not known). Converting the average log-layer diameter range reported by Carlier & Stanislas (2005) using $L = \sqrt{\pi}/2D$ yields $L = 35y_* - 44y_*$ while the present results indicate an average length-scale range $L = 45y_* - 52y_*$ over a similar wall-normal domain. While the present results are slightly larger than those reported by Carlier & Stanislas (2005), their PIV field of view was focused within the log layer which allowed a finer spatial resolution to be achieved. As such, their average core diameters are influenced by structures smaller than can be resolved in the present effort. Nevertheless, the vortices identified via Λ_{ci} have spatial characteristics consistent with previous observations in the literature.

4. Examples of prograde and retrograde spanwise vortices

Before discussing the quantitative population trends of prograde and retrograde spanwise vortices, instantaneous examples of these structures are considered. Figure 3(a) presents an instantaneous velocity realization in the streamwise–wall-normal plane of turbulent channel flow at $Re_\tau = 1185$ visualized via Galilean decomposition with a constant advection velocity of $0.81U_\infty$ removed (this advection velocity is 10% larger than the mean streamwise velocity at $y = 0.15\delta$, the wall-normal locus of the visualized cores). Galilean decomposition is used in this section since it provides a view of the local kinematics in the reference frame of the visualized structures. Seven spanwise vortices are noted within the log layer in this instantaneous field: five are prograde vortices (denoted A–E) and two are retrograde structures (labelled F and G). The prograde structures appear to induce strong ejections of low-speed fluid just below and upstream of their cores, consistent with the hairpin vortex signature introduced by Adrian *et al.* (2000). In addition, these prograde structures are aligned

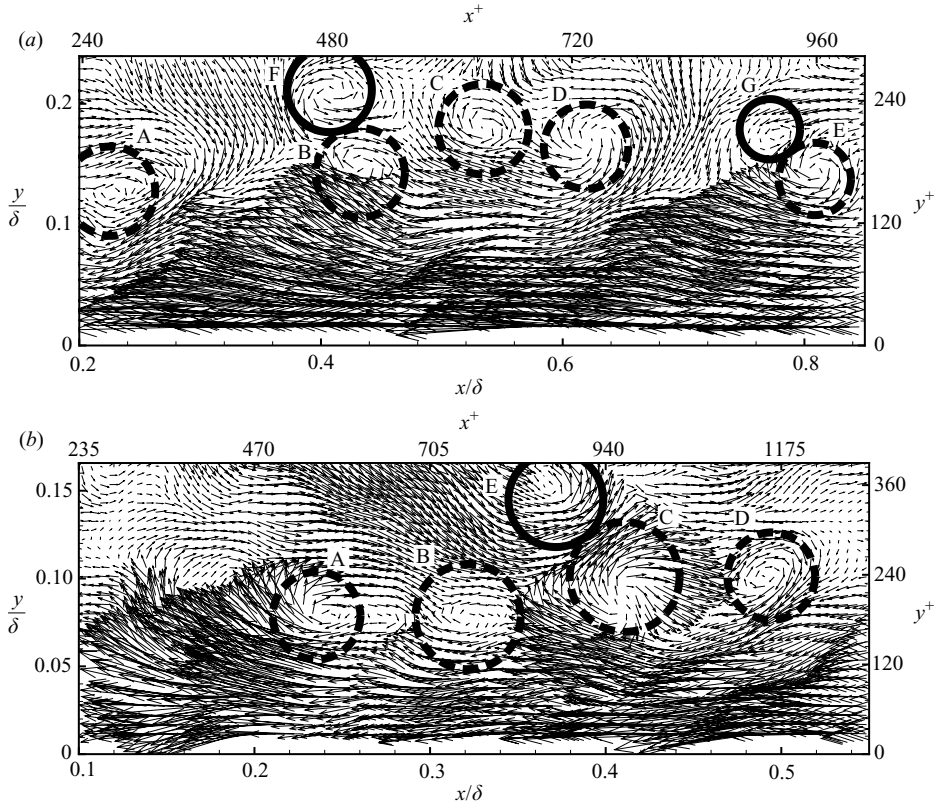

FIGURE 3. Examples of prograde and retrograde spanwise vortices via Galilean decomposition of instantaneous velocity fields in the streamwise–wall-normal plane of (*a*) turbulent channel flow at $Re_\tau = 1185$ and (*b*) a turbulent boundary layer at $Re_\tau = 2350$. Retrograde spanwise vortices are highlighted with solid circles; prograde vortices are highlighted with dashed circles.

in the streamwise direction, are slightly inclined away from the wall and are moving at nearly the same speed. As such, these hairpin vortices appear to form a vortex packet within the log layer and the collectively induced ejections generate a large-scale region of relatively uniform low-momentum fluid beneath the streamwise-aligned vortices, consistent with the packet observations of Adrian *et al.* (2000). Two retrograde structures, labelled F (spatially coincident with prograde structure B) and G (spatially coincident with prograde vortex E) are also noted in this Galilean decomposition. These retrograde spanwise vortices nest along the 'backbone' of the hairpin packet, similar to the scalar-visualization observations of Klewicki & Hirschi (2004).

Similar structural features are noted in figure 3(*b*) which presents an instantaneous velocity realization from the $Re_\tau = 2350$ boundary-layer ensemble visualized by Galilean decomposition with a constant advection velocity of $0.74U_\infty$ removed (15% larger than the mean streamwise velocity at $y = 0.1\delta$, the wall-normal locus of the visualized cores). Five spanwise vortices are revealed in this reference frame: four are prograde structures (labelled A–D) and the other is a retrograde structure (labelled E). The spatial characteristics of the prograde structures are consistent with the hairpin vortex signature of Adrian *et al.* (2000) and they are streamwise-aligned and inclined slightly away from the wall in the spirit of a hairpin packet. As in the channel-flow example, a retrograde vortex is noted in this realization and it nests along the outer

edge of the hairpin packet near prograde vortex C. In fact, the 'nesting' of retrograde structures in the vicinity of clusters of prograde vortices in and around the log layer is commonly observed in the vast majority of instantaneous velocity realizations in both flows. This behaviour is also clearly notable in the Λ_{ci} and local Galilean decomposition fields of figure 1.

Despite repeated observations of retrograde vortices nesting near prograde structures, it is impossible to infer the exact spatial relationships between these structures from instantaneous two-dimensional slices of the flow. This issue is further complicated by the fact that these flows are structurally active, particularly within the log layer. For example, one might argue that spatially coincident prograde and retrograde structures are in fact not isolated structures but instead form a counter-rotating pair in the spirit of Falco's typical eddy. However, the present data do not allow such a relationship to be confirmed and hence we can only report that retrograde structures often appear to cluster near prograde structures. Alternatively, these retrograde structures may be the by-product of the local dynamics of the hairpin vortices as postulated by Yang *et al.* (2001), the result of merging of hairpin structures as proposed by Tomkins & Adrian (2003) or simply the imprint of omega-shaped hairpin structures. Nevertheless, as will be seen in § 5, even if every retrograde structure is connected to a prograde vortex, streamwise-aligned prograde vortices with signatures consistent with hairpin structures still represent the majority of log-layer structure for the Re_τ range reported herein.

5. Population trends and characteristics of the vortices

5.1. *Vortex population densities*

Since the spatial location of each vortex is assessed from the instantaneous Λ_{ci} fields, the population trends of both prograde and retrograde spanwise vortices can be studied as a function of wall-normal position, Reynolds number and flow. The population density of prograde (retrograde) vortices, $\Pi_{p(r)}(y)$, is defined herein as the ensemble-averaged number of prograde (retrograde) spanwise vortices, $N_{p(r)}$, whose centres reside in rectangular areas of wall-normal height $3\Delta y/\delta$ and streamwise width L_x/δ centred at y, where L_x is the streamwise field of view for a given experiment. Therefore, $\Pi_{p(r)}(y)$ is given by

$$\Pi_{p(r)}(y/\delta) = \frac{N_{p(r)}(y/\delta)}{\dfrac{3\Delta y}{\delta}\dfrac{L_x}{\delta}}, \tag{5.1}$$

and represents the average number of prograde (retrograde) spanwise vortices per δ^2 area at a given y location – an outer-scaled population density. The use of an averaging window of height $3\Delta y/\delta$ decreases scatter in the profiles.

Figure 4(a) presents the outer-scaled prograde population densities, Π_p, as a function of y/δ for all channel and boundary-layer cases. The largest population densities of prograde spanwise vortices are seen close to the wall ($y < 0.3\delta$), with Π_p monotonically decreasing with y in both flows and at all Re_τ. This behaviour is similar to the instantaneous trends observed in figure 1(b) where the majority of prograde spanwise vortices reside in the region $y < 0.3\delta$. These wall-normal trends indicate that as prograde vortices grow away from the wall their average streamwise spacing may increase as they advect downstream. This observation is supported by Christensen *et al.* (2004) who found that the average streamwise spacing within outer-layer vortex organization increases with y. However, while it is probable that a portion of this

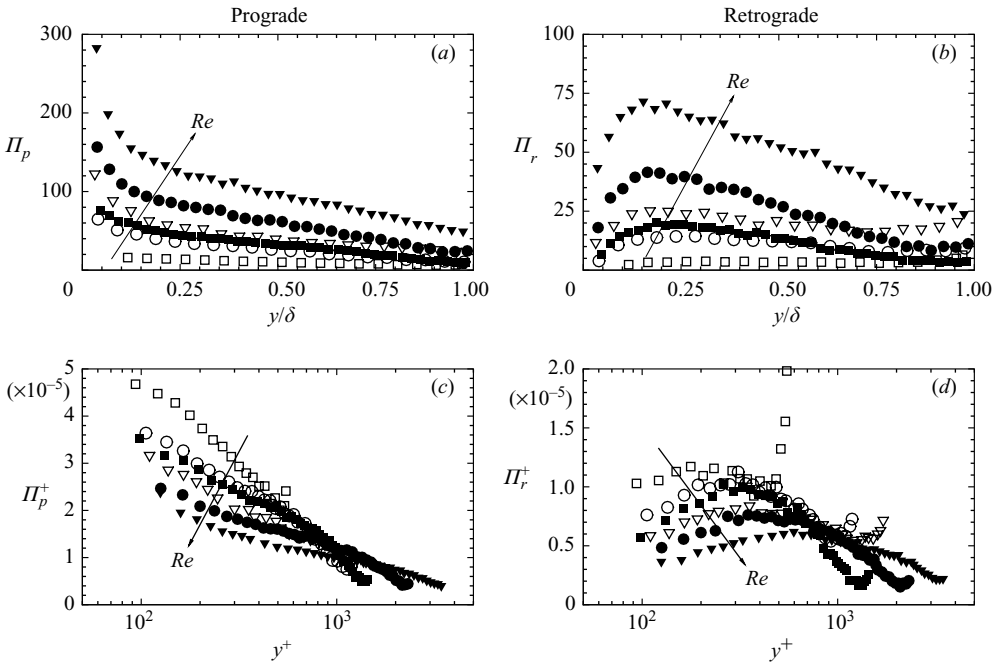

FIGURE 4. (*a*, *b*) Outer-scaled prograde and retrograde vortex population densities, Π_p and Π_r, versus y/δ. (*c*, *d*) Inner-scaled prograde and retrograde vortex population densities, Π_p^+ and Π_r^+, versus y^+. Symbols are defined in table 1 and not all data points shown for clarity.

wall-normal trend can be explained by the dispersion of prograde structures as they grow away from the wall, it is also supportive of the merging mechanisms proposed in the attached-eddy model of Perry & Chong (1982) and the near-wall scale-growth observations and outer-layer merging scenarios of Tomkins & Adrian (2003). For fixed wall-normal position in outer scaling, Π_p increases with Re_τ in both flows. This trend is not surprising since the diameters of these vortex cores appear to have inner-scale dependence (Carlier & Stanislas 2005). Therefore, a larger number of vortices per δ^2 area is possible with increasing Re_τ.

Figure 4(*b*) presents the outer-scaled population densities of retrograde spanwise vortices, Π_r, as a function of y/δ for all cases. In contrast to Π_p, Π_r grows steadily away from the wall to a local maximum near the outer edge of the log layer ($y \approx 0.2\delta$) in both flows and at all Re_τ. Beyond the log layer, Π_r decreases in both flows until approximately $y = 0.45\delta$ where it continues to decrease in the boundary layer. In channel flow, however, Π_r increases again and reaches a magnitude at $y = \delta$ that is comparable to its peak near $y = 0.2\delta$. Therefore, while the channel and boundary-layer flows exhibit similar Π_p trends for all y, the Π_r trends differ considerably for $y \gtrsim 0.45\delta$. These differences can be explained by noting that some fraction of the retrograde vortices in this region of channel flow may have their origin in the flow along the opposing wall. Retrograde spanwise vortices in the reference frame of the bottom wall of the channel are equivalently prograde spanwise vortices in the reference frame of the top wall (since the y-coordinate is reflected about the centreline). Therefore, the increase in Π_r for $y \gtrsim 0.45\delta$ may be attributable to prograde vortices from the flow along the top wall of the channel, possibly hairpin structures, that have advected across the centreline and joined the flow along the bottom wall. The

studies of Dean & Bradshaw (1976), Sabot & Compte-Bellot (1976) and Teitel & Antonia (1990), which indicate that the interaction region of turbulent channel flow has a wall-normal extent of $0.2\delta - 1.0\delta$ about the centreline, support this possibility. For fixed wall-normal position in outer scaling, Π_r increases with Re_τ in both flows, consistent with the Reynolds-number trends of Π_p.

Alternatively, an inner-scaled population density of prograde (retrograde) spanwise vortices can be computed as

$$\Pi^+_{p(r)}(y^+) = \frac{N_{p(r)}(y^+)}{3\Delta y^+ L^+_x}, \tag{5.2}$$

where $(\cdot)^+$ implies normalization by y_*. Therefore, $\Pi^+_{p(r)}(y^+)$ represents the average number of prograde (retrograde) spanwise vortices per y_*^2 area at a given y^+. Figure 4(c) presents Π^+_p versus y^+ for all channel and boundary-layer cases. As with Π_p, the inner-scaled prograde densities display clear Reynolds-number dependence. However, in contrast to Π_p which increases with increasing Re_τ, Π^+_p decreases with increasing Reynolds number in the log layer. The same Reynolds-number trend is noted in Π^+_r (figure 4d) where larger inner-scaled densities are observed at lower Re_τ in the log layer. Therefore, the average number of prograde and retrograde vortices per y_*^2 area decreases with increasing Reynolds number in the log layer. In addition, the peak in Π^+_r near the outer edge of the log layer clearly grows in y^+ with increasing Re_τ.

Since the outer- and inner-scaled prograde and retrograde population densities display clear Reynolds-number dependence, their Re_τ-dependence is assessed by postulating

$$\Pi_{p(r)} \sim Re_\tau^n, \tag{5.3}$$

for fixed y/δ. While suitable values of n were sought in an effort to collapse all six Re_τ cases, it was found that effective collapse was not achievable when the $Re_\tau = 570$ case was included in the analysis. Therefore, the Reynolds-number scaling exponents presented are assessed from the five higher-Re_τ cases. As shown in figure 5(a), the outer-scaled prograde population densities display $\Pi_p \sim Re_\tau^{1.17}$ dependence for $0.025 < y/\delta < 0.75$ with a slight deviation from this collapse for $y > 0.75\delta$. The $Re_\tau = 570$ channel-flow case deviates from this collapse for $y \lesssim 0.25\delta$, beyond which it collapses with the other Reynolds numbers. In contrast, the outer-scaled retrograde population densities display $\Pi_r \sim Re_\tau^{1.5}$ dependence for $y < 0.45\delta$ (figure 5b), beyond which the channel-flow and boundary-layer cases depart this scaling. As with the Π_p scaling, the $Re_\tau = 570$ case deviates in the region of collapse indicating that its structural characteristics are different from the higher Reynolds numbers. Note also that these Re_τ dependences are flow-insensitive as the channel and boundary-layer results follow the same trends in the regions of collapse.

The Reynolds-number dependence of the inner-scaled population densities is also considered for fixed y^+. The inner-scaled prograde population densities display $\Pi^+_p \sim Re_\tau^{-0.5}$ dependence (figure 5c), save for deviation of the $Re_\tau = 570$ case. This collapse is sustained within the wall-normal region $100 < y^+ < 0.5\delta^+$, beyond which successively higher Reynolds numbers deviate from the scaling. In contrast, the inner-scaled retrograde densities for the five higher Re_τ are found to display $\Pi^+_r \sim Re_\tau^{-0.64}$ dependence for $100 < y^+ < 0.2\delta^+$ (figure 5d). This wall-normal point of departure is consistent with the peak location of Π^+_r at $y^+ \approx 0.2\delta^+$. The anomalous behaviour of the $Re_\tau = 570$ case in these two scalings, coupled with its similar departure from the Re_τ-scalings of Π_p and Π_r, further supports the notion that the structural features

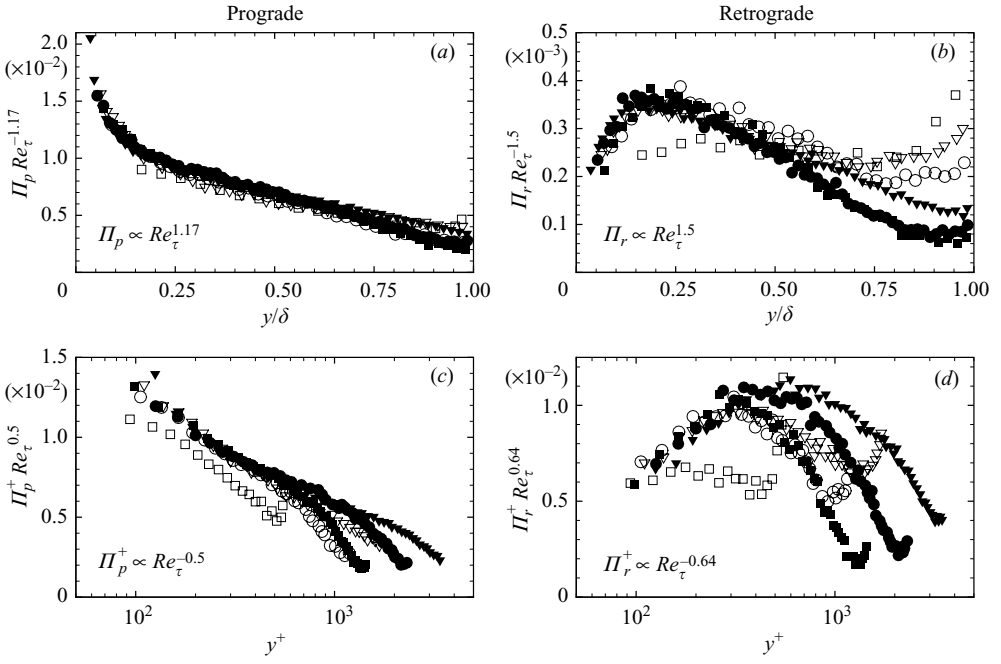

FIGURE 5. (a, b) Scaling of Π_p and Π_r with $Re_\tau^{1.17}$ and $Re_\tau^{1.5}$, respectively, versus y/δ. (c, d) Scaling of Π_p^+ and Π_r^+ with $Re_\tau^{-0.5}$ and $Re_\tau^{-0.64}$, respectively, versus y^+. Symbols are defined in table 1 and not all data points shown for clarity.

of this low-Re_τ case are different from the other higher-Re_τ cases, perhaps because it lacks a well-defined log layer.

5.2. *Vortex population fractions*

One can recast the population trends of the prograde and retrograde spanwise vortices in terms of the proportion of these structures that resides at a given wall-normal location:

$$\Psi_r(y) \equiv \frac{\Pi_r(y)}{\Pi_p(y) + \Pi_r(y)}, \tag{5.4}$$

where Ψ_r is the fraction of retrograde spanwise vortices and $\Psi_p(y) = 1 - \Psi_r(y)$ represents the fraction of prograde spanwise vortices at a given wall-normal location. Plots of Ψ_r are presented in figures 6(a) and 6(b) for all three channel-flow Re_τ as a function of y^+ and y/δ, respectively (Ψ_p is not shown since $\Psi_p = 1 - \Psi_r$). When plotted versus y^+, Ψ_r displays similarity, within the scatter in the data, up to $y^+ = 450$ for all three Re_τ, while the two higher Re_τ collapse up to $y^+ = 950$. Note that $y^+ = 450$ at $Re_\tau = 570$ and $y^+ = 950$ at $Re_\tau = 1185$ both correspond to $y^+ = 0.8\delta^+$. This behaviour indicates that the fraction of prograde and retrograde spanwise vortices exhibits similarity in channel flow through nearly the entire outer region versus y^+ for the Re_τ range reported. Similar collapse is not noted when Ψ_r is plotted versus y/δ, although a region of relative constancy for fixed Re_τ is observed for $0.25 < y/\delta < 0.75$ where the proportion of retrograde spanwise vortices increases slightly with Re_τ. For example, at $Re_\tau = 570$, 20%–25% of the spanwise vortices are retrograde, while at $Re_\tau = 1760$, 25%–30% are retrograde. The retrograde fractions converge to 0.5 at all

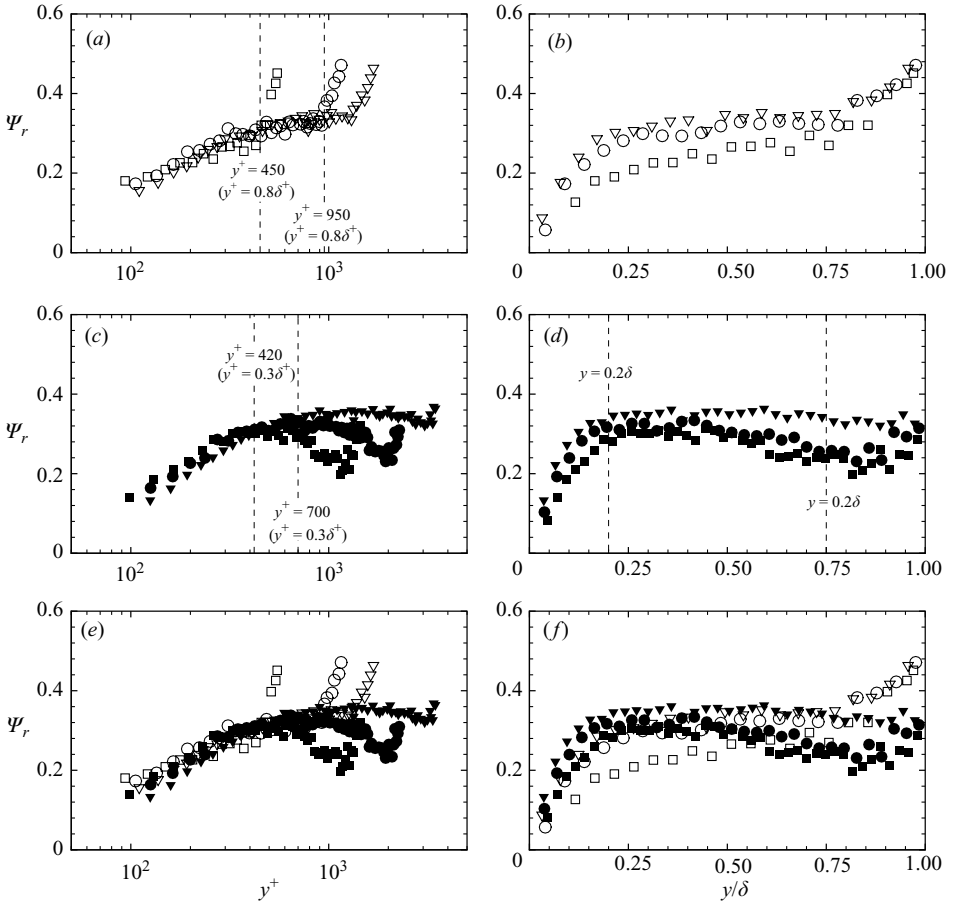

FIGURE 6. Fraction of retrograde spanwise vortices (Ψ_r) in (a, b) turbulent channel flow and (c, d) a turbulent boundary layer versus y^+ and y/δ, respectively. (e, f) Overlay of Ψ_r from both flows. Symbols are defined in table 1 and not all data points shown for clarity.

three Re_τ as the centerline is approached, consistent with the symmetry of channel flow about its centreline.

Figures 6(c) and 6(d) present Ψ_r at all three boundary-layer Re_τ versus y^+ and y/δ, respectively. In contrast to the channel-flow retrograde fractions, Ψ_r exhibits similarity for a reduced y^+ range in the boundary layer, with the $Re_\tau = 1400$ fraction departing this collapse near $y^+ = 420$ and the $Re_\tau = 2350$ fraction departing near $y^+ = 700$. These points of departure both correspond to $y^+ = 0.3\delta^+$, indicating that similarity in Ψ_p and Ψ_r does not extend far beyond the log layer of the turbulent boundary layer. When plotted versus y/δ, Ψ_r decreases slowly in the region $0.25 < y/\delta < 0.75$ of the boundary layer, but grows slightly with Reynolds number in this range, most notably in the wake region where the growth rate of Ψ_r with Re_τ is positive and increasing.

Figures 6(e) and 6(f) show overlays of Ψ_r from the channel and boundary-layer cases versus y^+ and y/δ, respectively. The retrograde fractions collapse along a similar path irrespective of flow and Re_τ for $100 < y^+ < 0.3\delta^+$ when plotted versus y^+, beyond which the boundary-layer cases depart from this similarity. The slight scatter that exists between the boundary-layer and channel-flow data is well within the error bounds of using the Clauser chart method to determine u_* and y_* for the

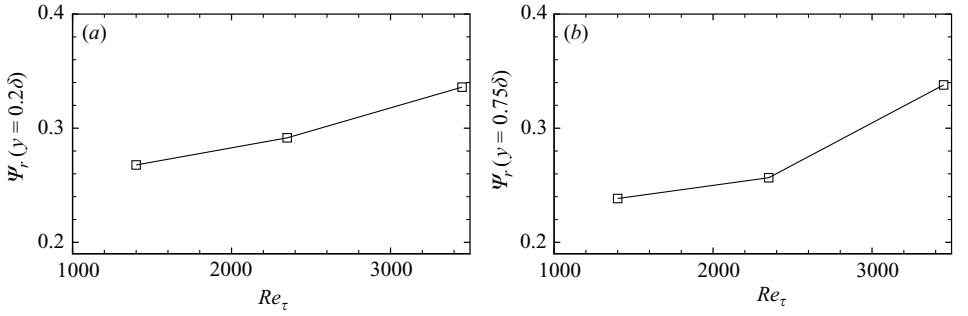

FIGURE 7. Fraction of retrograde spanwise vortices (Ψ_r) in the boundary layer versus Re_τ at (*a*) $y = 0.2\delta$ and (*b*) $y = 0.75\delta$.

boundary-layer experiments and could also be associated with the fact that the boundary-layer data are slightly less resolved in inner units ($11y_*$ versus $9y_*$ (channel)). Nevertheless, a clear consistency in Ψ_r exists between the two flows in the region $100 < y^+ < 0.3\delta^+$. The channel and boundary-layer retrograde fractions display Re_τ dependence when plotted versus y/δ, with the $Re_\tau = 3450$ boundary-layer data having the largest values of Ψ_r for $y < 0.75\delta$ and the $Re_\tau = 570$ channel data displaying the smallest.

As noted earlier, the $Re_\tau = 570$ channel-flow case appears to suffer from low-*Re* effects, meaning that channel-flow cases cannot be faithfully used to assess the growth of Ψ_r with Reynolds number in the outer layer. However, the boundary-layer cases do not suffer in this regard and can therefore be utilized for such purposes. Figure 7(*a*) presents Ψ_r for the boundary-layer cases as a function of Re_τ near the outer edge of the log layer ($y = 0.2\delta$). The retrograde vortex fraction at $y = 0.2\delta$ has a positive and slightly increasing growth rate ($\partial\Psi_r/\partial Re_\tau > 0$; $\partial^2\Psi_r/\partial Re_\tau^2 > 0$) over the Re_τ range reported. More rapid growth in Ψ_r with Re_τ is noted near the edge of the boundary layer at $y = 0.75\delta$ (figure 7*b*). These two examples illustrate that the prevalence of retrograde vortices increases with increasing Re_τ over the Reynolds-number range reported throughout the outer layer of the boundary layer, with the most rapid growth occurring in the wake region. Unfortunately, it cannot be determined from the present data to what values Ψ_p and Ψ_r might saturate at some higher Reynolds number. However, the present results clearly illustrate that retrograde spanwise vortices become increasing prevalent outside the log layer at higher Reynolds numbers with a commensurate relative decrease in the incidence of prograde structures outside the log layer.

5.3. *Channel and boundary-layer population trends at comparable* Re_τ

The similarities and differences between channel and boundary-layer flows can be further assessed by contrasting the population trends of prograde and retrograde spanwise vortices at comparable Re_τ. Figure 8(*a*) presents Π_p and Π_r for the $Re_\tau = 1185$ channel and $Re_\tau = 1400$ boundary-layer cases. The prograde population densities collapse for all wall-normal locations save for a slight deviation near $y = \delta$. In contrast, the retrograde population densities collapse for $y < 0.45\delta$, beyond which Π_r continues to decrease in the boundary layer while increasing again near $y = \delta$ in channel flow. This disparity in Π_r for $y > 0.45\delta$ is therefore responsible for differences between the fraction of retrograde vortices, Ψ_r, of the channel and boundary-layer cases (figure 8*b*). As was noted earlier, the increase in Π_r and Ψ_r near the centreline of

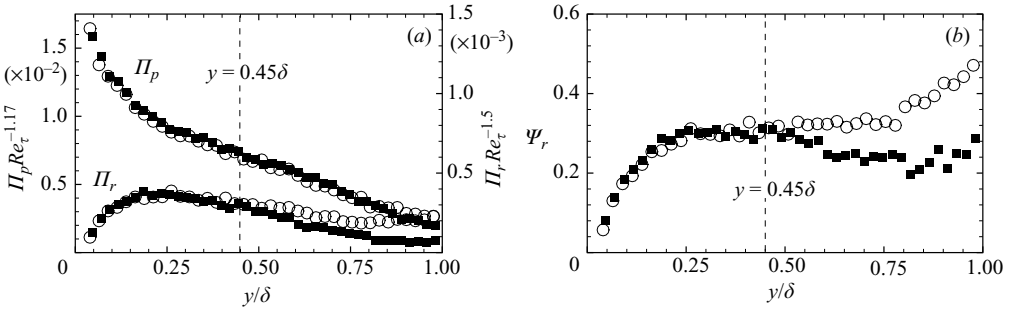

FIGURE 8. Comparison of channel flow ($Re_\tau = 1185$) and boundary layer ($Re_\tau = 1400$) (*a*) population densities (Π_p and Π_r) and (*b*) retrograde vortex fractions (Ψ_r). Symbols are defined in table 1 and not all data points shown for clarity.

channel flow is most likely due to prograde structures in the reference frame of the top wall that have crossed the centreline to join the flow along the bottom wall as retrograde structures. Based on similar arguments, one would expect a deficit of prograde vortices in channel flow near $y = \delta$, compared to the boundary layer, since presumably some of the prograde structures in the reference frame of the bottom wall cross the centreline to join the flow along the top wall. However, the prograde populations near $y = \delta$ can also be enhanced by retrograde structures in the reference frame of the top wall that may cross the centreline and join the flow along the bottom wall. This cross-population of structures across the centreline accounts for the slightly larger values of Π_p near $y = \delta$ in channel flow compared to the boundary layer. Nevertheless, the noted consistency in Π_p, Π_r and Ψ_r for $y < 0.45\delta$ indicates that the structural features of these flows are essentially the same in the lower half of both flows. As such, the present results suggest that the region $\pm 0.55\delta$ about the centreline can be regarded as a region where structures from both walls coexist. This estimate of the interaction region is larger than that cited by Dean & Bradshaw (1976) ($\pm 0.2\delta$) and Sabot & Compte-Bellot (1976) ($\pm 0.3\delta$) but smaller than the observations of Teitel & Antonia (1990) which indicated that events originating at one wall can often reach the inner layer of the opposing wall.

5.4. *Contributions to mean shear*

The contributions of prograde and retrograde spanwise vortices to the overall mean shear are also assessed from the PIV ensembles. The total mean shear is given by

$$\tau(y) = \mu \frac{\partial U}{\partial y} - \rho \langle u'v' \rangle, \tag{5.5}$$

where the first term on the right-hand side represents the mean viscous shear and the second term embodies the shear contributions due to turbulent stresses (primes denote fluctuating quantities). The contributions of prograde (retrograde) spanwise vortex cores to $\tau(y)$ can be computed as a stress fraction of the form

$$S_{p(r)}(y) \equiv \frac{\tau_{p(r)}(y)}{\tau(y)}, \tag{5.6}$$

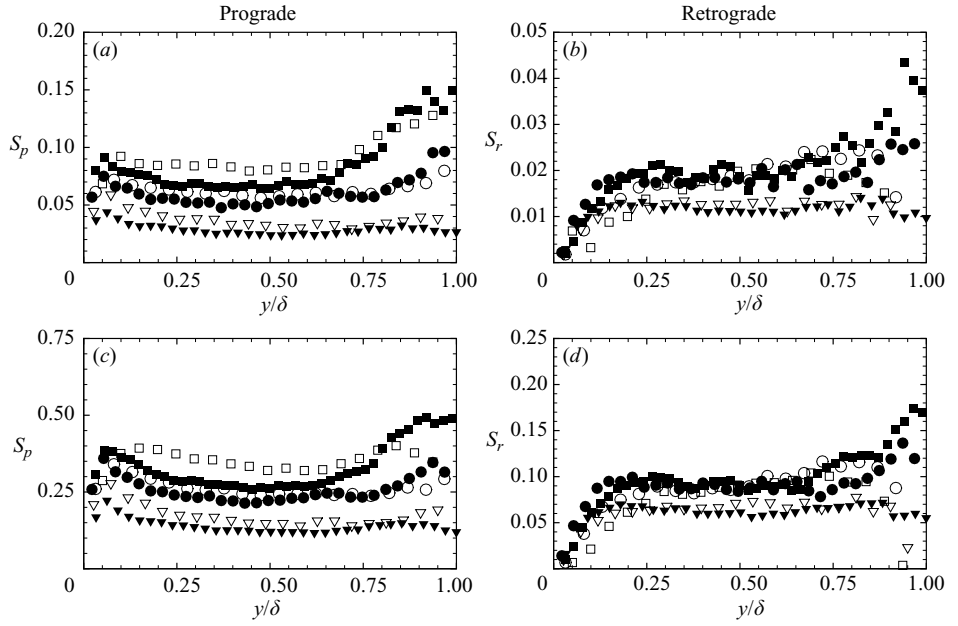

FIGURE 9. (a, b) Fraction of mean shear contained within prograde and retrograde vortex cores, respectively. (c, d) Fraction of mean shear associated with cores and locally induced motions for prograde and retrograde structures, respectively. Symbols are defined in table 1 and not all data points shown for clarity.

where

$$\tau_{p(r)}(y) = \frac{1}{M}\sum_{i=1}^{M}\left(\mu\frac{\partial u}{\partial y} - \rho u'v'\right)\Big|_{(x_i,y)} I_{p(r)}(x_i, y) \tag{5.7}$$

represents the mean shear contained within the cores of prograde (retrograde) vortices at a given y (Here $M = N_e N_x$, where N_e is the number of realizations in a given ensemble and N_x is the number of streamwise grid points in each velocity realization of that ensemble.). The indicator function, $I_{p(r)}(x_i, y)$, is given as

$$I_{p(r)}(x_i, y) = \begin{cases} 1 & \text{if } (x_i, y) \text{ is within an identified prograde (retrograde) core,} \\ 0 & \text{otherwise.} \end{cases} \tag{5.8}$$

and distinguishes grid points that fall within the boundaries of the identified prograde (retrograde) vortex cores from all others. Therefore, the total fractional contribution of spanwise vortex cores to the mean shear is $S_p + S_r$. These stress fractions represent lower bounds on the mean-shear contributions of these vortices since they only account for the mean shear contained within the cores themselves and not shear induced by the cores.

Figure 9(a) presents the mean-shear contributions of prograde spanwise vortex cores, S_p, as a function of wall-normal position for both the channel and boundary-layer datasets. The contributions reach a local maximum close to the wall for fixed Re_τ and decline slightly to a region of relative constancy for $0.25 < y/\delta < 0.75$, beyond which they increase again. The peak in prograde mean-shear contributions close to the wall is coincident with the largest populations of prograde spanwise vortices

as noted earlier (figure 4). An outer-layer Reynolds-number trend is evident, with prograde cores contributing a larger fraction to the mean shear at lower Re_τ (8%–9% for the $Re_\tau = 570$ channel-flow case compared to 3%–4% for the $Re_\tau = 3450$ boundary-layer case). This outer-layer Reynolds-number trend is consistent with that of the prograde vortex fractions (figure 6). In contrast, the retrograde vortex cores contribute very little to the mean shear (figure 9*b*), particularly close to the wall where their contributions are less than 1% over the Re_τ range reported herein. The retrograde mean-shear contributions reach a maximum of 1%–2% near $y = 0.2\delta$, consistent with the log-layer peak in their population densities. In addition, S_r is found to be positive, indicating that the Reynolds-stress contributions of retrograde cores dominate over their viscous contributions to the mean shear, even close to the wall. As with S_p, S_r attains a region of relative constancy for $0.25 < y/\delta < 0.75$ and decreases with increasing Reynolds number. As such, while the population fraction of retrograde cores increases with increasing Re_τ in the outer layer (figure 6), their contributions to the mean shear decrease with increasing Re_τ.

While the prograde and retrograde vortex cores contribute little to the overall mean shear, particularly with increasing Re_τ, the instantaneous realizations presented herein suggest that the motions induced by these cores can generate significant instantaneous shear. Therefore, the mean-shear contributions of both the cores and the induced-motions in the immediate vicinity of the cores are estimated by centring a bounding box on each vortex core with sides two grid points larger than the extent of the vortex core in each direction as determined by the $|\widetilde{\Lambda}_{ci}| \geqslant 1.5$ threshold. Care is taken to ensure that these induced motions are included only once in the calculation as it is possible that the bounding box of one vortex may overlap that of a neighbouring vortex. These core and induced-flow mean-shear contributions are presented in figures 9(*c*) and 9(*d*) for prograde and retrograde vortices, respectively. While their qualitative wall-normal and Reynolds-number trends are identical to those observed for the core contributions alone, inclusion of the induced motions in the immediate vicinity of the cores increases the mean-shear contributions by a factor of 4–5 for both retrograde and prograde vortices. Therefore, while the vortex cores themselves contribute very little to the overall mean shear, the motions induced by these structures can generate significant shear.

5.5. *Advection velocities*

Finally, since the location of each spanwise vortex is identified in the present effort, the instantaneous streamwise advection velocities of the vortices can also be assessed. Figures 10(*a*) and 10(*b*) present the mean advection velocities, U_c, of both prograde and retrograde spanwise vortices as a function of wall-normal position for the $Re_\tau = 1760$ channel-flow and $Re_\tau = 2350$ boundary-layer cases, respectively (For brevity, only these two Reynolds numbers are presented as the other channel and boundary-layer cases exhibit similar trends). On average, both prograde and retrograde spanwise vortices are advected with the mean streamwise velocity in both flows, consistent with the recent log-layer results of Carlier & Stanislas (2005) (although they did not differentiate between the advection velocities of prograde and retrograde structures). However, while the mean advection velocities of these vortices collapse on the local streamwise mean, the distributions of advection velocities about the mean exhibit strong wall-normal dependence. Histograms of the prograde and retrograde advection velocities at three different wall-normal locations are presented in figure 10(*c–e*) for the channel-flow case and figure 10(*f–h*) for the boundary-layer case. These histograms have broad widths at the inner boundary of the log layer, with some prograde and

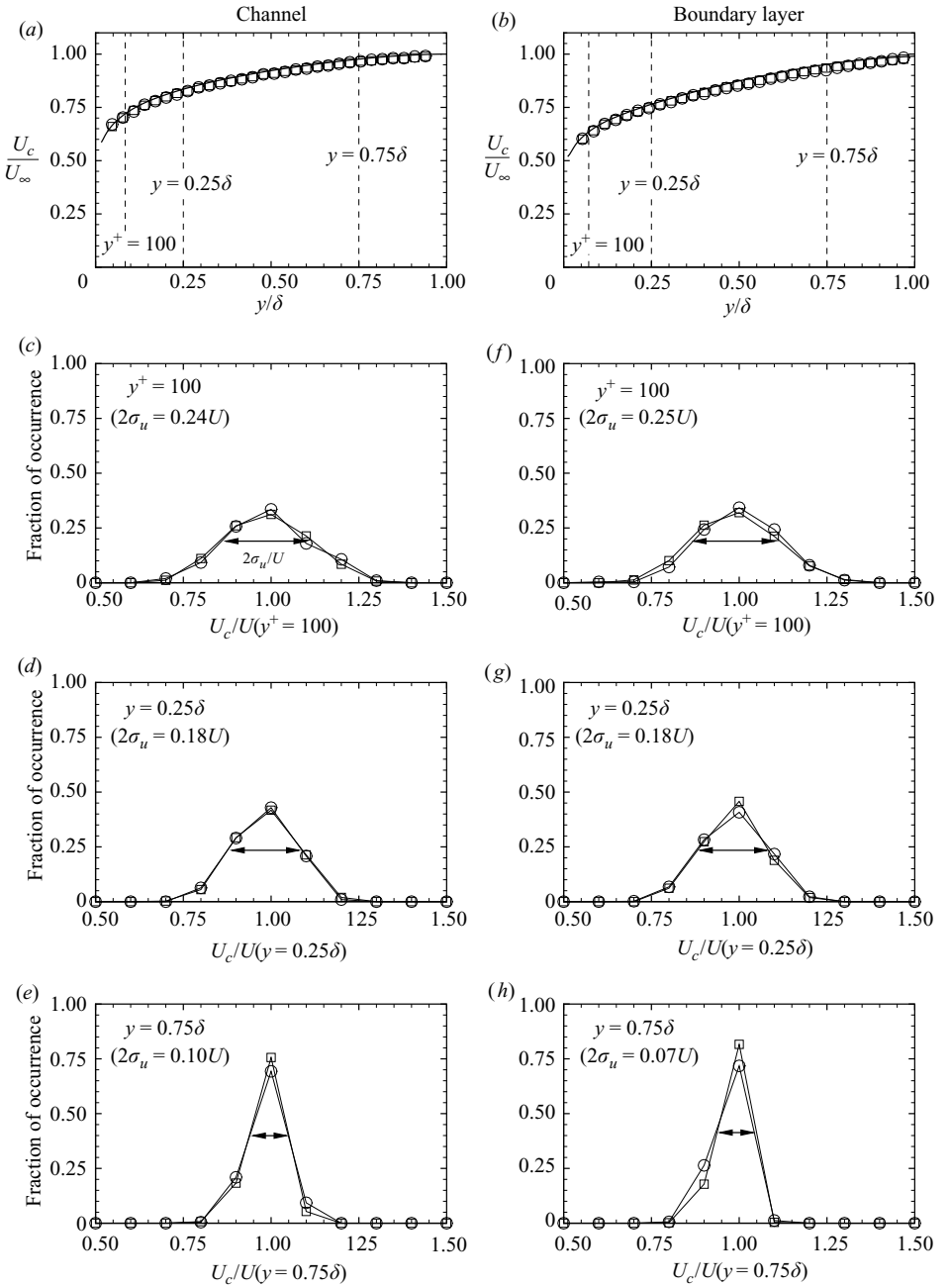

FIGURE 10. Mean advection velocities of prograde and retrograde spanwise vortices versus y/δ in (*a*) turbulent channel flow at $Re_\tau = 1760$ and (*b*) a turbulent boundary layer at $Re_\tau = 2350$. Solid lines represent the mean velocity profiles. (*c*)–(*e*) Histograms of prograde and retrograde vortex advection velocities at $y^+ = 100$, $y = 0.25\delta$ and $y = 0.75\delta$ for the case shown in (*a*); (*f*–*h*) Histograms of prograde and retrograde vortex advection velocities at $y^+ = 100$, $y = 0.25\delta$ and $y = 0.75\delta$ for the case shown in (*b*). Arrows in (*c*–*h*) represent the $2\sigma_u$ width of p.d.f.s for each wall-normal location. □, Prograde; ○, Retrograde.

retrograde structures advecting as much as 30% faster or slower than the local mean in both flows. The widths of the histograms decrease slightly with increasing y but are still relatively broad even at the outer edge of the log layer. Farther away from the wall at $y = 0.75\delta$, the histograms become much narrower with most of the structures advecting within 10%–15% of the local streamwise mean. Interestingly, the widths of the histograms are found to be proportional to the local RMS streamwise velocity, σ_u. Therefore, while both prograde and retrograde spanwise vortices travel on average with the local mean velocity, their instantaneous advection velocities are strongly influenced by the local turbulence levels, particularly close to the wall.

6. Conclusions

The results presented indicate that prograde and retrograde spanwise vortices occur frequently throughout both turbulent channel flow and the zero-pressure-gradient turbulent boundary layer, with the largest populations existing in the region $100 < y^+ < 0.25\delta^+$: the log layer. In particular, the inner boundary of the log layer in both channel and boundary-layer flows is densely populated by prograde spanwise vortices that have characteristics consistent with the heads of hairpin vortices, the building-blocks of outer-layer vortex organization (Adrian *et al.* 2000). The log layer is also populated by many retrograde spanwise vortices, with their maximum populations occurring near the outer edge of the log layer ($y \approx 0.2\delta$) in both turbulent channel and boundary-layer flows. While their origin cannot be inferred from instantaneous two-dimensional snapshots of the flow, these retrograde structures are often observed to nest near clusters of prograde vortices that form hairpin vortex packets. However, while both channel flow and the boundary layer show identical retrograde-vortex population trends in the log layer, these flows differ considerably in this regard for $y > 0.45\delta$. In particular, both the population density and fraction of retrograde vortices decrease with wall-normal position beyond the log layer in the boundary layer while these quantities increase with y in channel flow near its centreline. Such differences are likely to be associated with the influence of the opposing wall in channel flow whereby prograde structures in the reference frame of the top wall appear as retrograde vortices in the reference frame of the bottom wall. Therefore, the region $\pm 0.55\delta$ about the centreline of channel flow can be regarded as an interaction region where structures from both walls commonly exist. Nevertheless, the structural populations of channel flow and the boundary layer are found to be the same below this interaction region for similar Re_τ.

The outer-scaled population densities of resolved prograde vortices show $Re_\tau^{1.17}$ dependence in both flows throughout the outer layer versus y/δ while the outer-scaled retrograde densities display $Re_\tau^{1.5}$ dependence for $y < 0.45\delta$. In contrast, the inner-scaled prograde densities exhibit $Re_\tau^{-0.5}$ dependence for $100 < y^+ < 0.5\delta^+$ while the inner-scaled retrograde densities display $Re_\tau^{-0.64}$ dependence for $100 < y^+ < 0.2\delta^+$. The $Re_\tau = 570$ channel-flow case deviates from each of these scalings, particularly in the cases of Π_r and Π_r^+, perhaps because it lacks a well-defined log layer. When the population densities are recast in terms of fractions of prograde and retrograde structures, similarity is noted within the log layer when plotted versus y^+. This behaviour is found to be flow-independent, as the results from both channel flow and the boundary layer collapse along the same path for $100 < y^+ < 0.3\delta^+$. In addition, the proportion of retrograde spanwise vortices grows slightly with Re_τ in both flows for $y > 0.25\delta$, indicating that retrograde structures may play an increasingly important role at higher Reynolds numbers. This behaviour is most prominent in the wake

region of the turbulent boundary layer where the growth rate of the retrograde vortex fraction with Reynolds number is positive and increasing ($\partial\Psi_r/\partial Re_\tau > 0$; $\partial^2\Psi_r/\partial Re_\tau^2 > 0$).

Finally, prograde and retrograde cores travel, on average, with the local mean velocity, although their instantaneous advection velocities can be significantly altered by the local turbulence levels. In addition, prograde and retrograde cores contribute very little to the overall mean shear. However, the motions induced by these vortices do make significant contributions in this regard, particularly in the case of prograde structures which can contribute between 20% and 40%, with larger contributions occurring at lower Re_τ.

The authors gratefully acknowledge the insightful comments of the reviewers. The channel-flow experiments were performed during the second author's tenure at the University of New Mexico with funding from Oak Ridge Associated Universities via a Junior Faculty Enhancement Award. The boundary-layer work was performed at the University of Illinois with funding from the Air Force Office of Scientific Research under Grants FA9550-05-1-0043 and FA9550-05-1-0246 (Dr John Schmisseur, Program Manager).

REFERENCES

Adrian, R. J., Meinhart, C. D. & Tomkins, C. D. 2000 Vortex organization in the outer region of the turbulent boundary layer. *J. Fluid Mech.* **422**, 1–54.

Brooke, J. W. & Hanratty, T. J. 1993 Origin of turbulence-producing eddies in a channel flow. *Phys. Fluids* A **5** (4), 1011–1022.

Carlier, J. & Stanislas, M. 2005 Experimental study of eddy structures in a turbulent boundary layer using particle image velocimetry. *J. Fluid Mech.* **535**, 143–188.

Chakraborty, P., Balachandar, S. & Adrian, R. J. 2005 On the relationships between local vortex identification schemes. *J. Fluid Mech.* **535**, 189–214.

Chong, M. S., Perry, A. E. & Cantwell, B. J. 1990 A general classification of three-dimensional flow fields. *Phys. Fluids* A **2** (5), 765–777.

Christensen, K. T., Wu, Y., Adrian, R. J. & Lai, W. 2004 Statistical imprints of structure in wall turbulence, *AIAA* Paper 2004-1116.

Dean, R. B. & Bradshaw, P. 1976 Measurements of interacting turbulent shear layers in a duct. *J. Fluid Mech.* **78**, 641–676.

Delo, C. J., Kelso, R. M. & Smits, A. J. 2004 Three-dimensional structure of a low-Reynolds-number turbulent boundary layer. *J. Fluid Mech.* **512**, 47–83.

Falco, R. E. 1977 Coherent motions in the outer region of turbulent boundary layers. *Phys. Fluids* **20** (10), S124–S132.

Falco, R. E. 1983 New results, a review and synthesis of the mechanism of turbulence production in boundary layers and its modification. *AIAA Paper* 83-0377.

Falco, R. E. 1991 A coherent structure model of the turbulent boundary layer and its ability to predict Reynolds number dependence. *Phil. Trans. R. Soc. Lond.* A **336**, 103–129.

Ganapathisubramani, B., Longmire, E. K. & Marusic, I. 2003 Characteristics of vortex packets in turbulent boundary layers. *J. Fluid Mech.* **478**, 35–46.

Head, M. R. & Bandyopadhyay, P. 1981 New aspects of turbulent boundary-layer structure. *J. Fluid Mech.* **107**, 297–338.

Klewicki, J. C. 1997 Self-sustaining traits of near-wall motions underlying boundary layer stress transport. In *Self-Sustaining Mechanisms of Wall Turbulence* (ed. R. L. Panton), chap. 7, pp. 135–166. Computational Mechanics Publications.

Klewicki, J. C., Gendrich, C. P., Foss, J. F. & Falco, R. E. 1990 On the sign of the instantaneous spanwise vorticity component in the near-wall region of turbulent boundary layers. *Phys. Fluids* A **2** (8), 1497–1500.

Klewicki, J. C. & Hirschi, C. R. 2004 Flow field properties local to near-wall shear layers in a low Reynolds number turbulent boundary layer. *Phys. Fluids* **16** (11), 4163–4176.

Kline, S. J. & Robinson, S. K. 1989 Quasi-coherent structures in the turbulent boundary layer. Part 1: Status report on a community-wide summary of the data. In *Near Wall Turbulence* (ed. S. J. Kline & N. H. Afgan), pp. 218–247. Hemisphere.

Liu, Z.-C., Adrian, R. J. & Hanratty, T. J. 2001 Large-scale modes of turbulent channel flow: Transport and structure. *J. Fluid Mech.* **448**, 53–80.

Meinhart, C. D. 1994 Investigation of turbulent boundary-layer structure using particle-image velocimetry. PhD thesis, Department of Theoretical and Applied Mechanics, University of Illinois at Urbana-Champaign.

Melander, M. V. & Zabuski, N. J. 1988 Interaction and apparent reconnection of 3D vortex tubes via direct numerical simulations. *Fluid Dyn. Res.* **3**, 247–250.

Moin, P., Leonard, A. & Kim, J. 1986 Evolution of a curved vortex filament into a vortex ring. *Phys. Fluids* **29**, 955–963.

Nagaosa, R. & Handler, R. A. 2003 Statistical analysis of coherent vortices near a free surface in a fully developed turbulence. *Phys. Fluids* **15** (2), 375–394.

Perry, A. E. & Chong, M. S. 1982 On the mechanism of wall turbulence. *J. Fluid Mech.* **119**, 173–217.

Sabot, J. & Compte-Bellot, G. 1976 Intermittency of coherent structures in the core region of fully developed turbulent pipe flow. *J. Fluid Mech.* **74**, 767–796.

Schoppa, W. & Hussain, F. 1997 Genesis and dynamics of coherent structures in near-wall turbulence: A new look. In *Self-Sustaining Mechanisms of Wall Turbulence* (ed. R. L. Panton), chap. 16, pp. 385–422. Computational Mechanics Publications.

Smith, C. R. 1984 A synthesized model of the near-wall behavior in turbulent boundary layers. In *Proc. 8th Symp. on Turbulence*, pp. 299–325. University of Missouri-Rolla, Rolla, Missouri.

Smith, C. R., Walker, J. D. A., Haidari, A. H. & Sobrun, U. 1991 On the dynamics of near-wall turbulence. *Phil. Trans. R. Soc. of Lond.* A **336**, 131–175.

Teitel, M. & Antonia, R. A. 1990 The interaction region of a turbulent duct flow. *Phys. Fluids* A **2** (5), 808–813.

Theodorsen, T. 1952 Mechanism of turbulence. In *Proc. 2nd Midwestern Conf. on Fluid Mechanics*, pp. 1–19. Ohio State University, Columbus.

Tomkins, C. D. & Adrian, R. J. 2003 Spanwise structure and scale growth in turbulent boundary layers. *J. Fluid Mech.* **490**, 37–74.

Yang, M., Meng, H. & Sheng, J. 2001 Dynamics of hairpin vortices generated by a mixing tab in a channel flow. *Exps. Fluids* **30**, 705–722.

Zhou, J., Adrian, R. J., Balachandar, S. & Kendall, T. M. 1999 Mechanisms for generating coherent packets of hairpin vortices in channel flow. *J. Fluid Mech.* **387**, 353–396.